sensors

MDPI

Article

Photoacoustic-MR Image Registration Based on a Co-Sparse Analysis Model to Compensate for Brain Shift

Parastoo Farnia[1,2], Bahador Makkiabadi [1,2], Maysam Alimohamadi[3], Ebrahim Najafzadeh[1,2], Maryam Basij[4], Yan Yan[4], Mohammad Mehrmohammadi [4,5], and Alireza Ahmadian[1,2, *]

[1] Medical Physics and Biomedical Engineering Department, Faculty of Medicine, Tehran University of Medical Sciences (TUMS), Tehran, Iran.
[2] Research Centre of Biomedical Technology and Robotics (RCBTR), Imam Khomeini Hospital Complex, Tehran University of Medical Sciences, Tehran, Iran.
[3] Brain and spinal cord injury research center, Neuroscience Institute, Tehran University of Medical Sciences (TUMS), Tehran, Iran.
[4] Department of Biomedical Engineering, Wayne State University, Detroit, Michigan, USA.
[5] Barbara Ann Karmanos Cancer Institute, Detroit, Michigan, USA.
* Correspondence: ahmadian@sina.tums.ac.ir

Abstract: Brain shift is an important obstacle to the application of image guidance during neurosurgical interventions. There has been a growing interest in intra-operative imaging to update the image-guided surgery systems. However, due to the innate limitations of the current imaging modalities, accurate brain shift compensation continues to be a challenging task. In this study, the application of intra-operative photoacoustic imaging and registration of the intra-operative photoacoustic with pre-operative MR images is proposed to compensate for brain deformation. Finding a satisfactory registration method is challenging due to the unpredictable nature of brain deformation. In this study, the co-sparse analysis model is proposed for photoacoustic -MR image registration, which can capture the interdependency of the two modalities. The proposed algorithm works based on the minimization of the mapping transform via a pair of analysis operators that are learned by the alternating direction method of multipliers. The method was evaluated using experimental phantom and ex-vivo data obtained from the mouse brain. The results of phantom data show about 63% improvement in target registration error in comparison with the commonly used normalized mutual information method. Results proved that intra-operative photoacoustic images could become a promising tool when the brain shift invalidated pre-operative MRI.

Keywords: brain shift; photoacoustic imaging; multimodal image registration; dictionary learning; co-sparse analysis.

Citation: Lastname, F.; Lastname, F Lastname, F. Title. *Sensors* **2021**, *21*, x. https://doi.org/10.3390/xxxx

Academic Editor: Firstname Lastname

Received: date
Accepted: date
Published: date

1. Introduction

Maximal Safe resection of brain tumors in eloquent regions is optimally performed under image-guided surgery systems [1,2]. The accuracy of the image-guided neurosurgery system is drastically affected by intra-operative tissue deformation, called brain shift. Brain shift is a dynamic and complex spatiotemporal phenomenon that happens after performing a craniotomy and invalidates the pre-operative image of patients [3,4]. The brain shift, which is known as brain deformation, is a combination of a wide variety of biological, physical, and surgical causes and occurs in both cortical and deep brain structures [2,5-7]. Brain shift calculation and compensation methods are based on updating the pre-operative images with regard to the intraoperative tissue deformation. These methods fall into two main categories: biomechanical models and intra-operative imaging approaches. Biomechanical model-based approaches are time and computation-consuming methods; however, they could be highly accurate [8-10]. The main drawback of model-based techniques is that tissue deformation that occurs during intraoperative neurosurgical procedures is difficult to accurately model in real-time processes and thus is often not considered [2]. As a result, most of the recent studies have focused on using intra-operative imaging, including intraoperative computed tomography (CT) [11], magnetic resonance imaging (MRI) [12-14], fluorescence-guided surgery

[15], and ultrasound (US) imaging [16-18] during neurosurgery. In fact, interventional imaging systems are becoming an integral part of modern neurosurgeries to update patient's coordinate during surgery using registration of intra-operative images with pre-operative images [19]. However, each of these modalities has been proven to have well-known limitations [20]. Radiation exposure and low spatial resolution in CT, the requirement for an expensive equipped MR compatible operating room, and time-consuming imaging in MRI, limited imaging depth in fluorescence imaging, and poor quality of the US images are the major challenges of the common intra-operative imaging modalities [21].

Recently, the application of hybrid imaging modalities such as photoacoustic (PA) imaging has gained considerable interest for various applications such as differential diagnostic of pathologies [22,23], depicting tissue vasculature [24], oral health [25,26] and image-guided surgeries [27-29]. The PA is a non-ionizing hybrid imaging method that combines optical and ultrasound imaging modalities based on the PA effect: the formation of sound waves following pulsed light absorption in a medium [30-32]. PA imaging inherits the advantages of high imaging contrast from optical imaging as well as the spatial and temporal resolution of US imaging [33-37]. During PA image acquisition, the tissue is illuminated by short laser pulses, which are absorbed by endogenous (or exogenous) chromophores and cause the generation of ultrasound emission due to thermoelastic expansion. Endogenous chromophores such as hemoglobin provide a strong PA signal due to high optical absorption coefficients, which in turn demonstrate the crucial structural information [30,38]. One of the main advantages of PA imaging is the ability to visualize the blood vessel meshwork of brain tissue, which is considered as the main landmark during neurosurgery [21,39,40]. On the other hand, PA imaging has demonstrated the potential to be used during image-guided interventions [41-43]. As a result, PA imaging as a noninvasive intra-operative imaging could enable the real-time visualization of regions of interest including vessel meshwork during neurosurgery. Finally, registration of intra-operative PA images with pre-operative MR images of brain tissue could enable real-time compensation of brain shift.

Many investigations have tried to overcome the limitations of multimodal image registration algorithms in processes of brain shift compensation. Nevertheless, finding a single satisfactory solution is a challenging task due to the complex and unpredictable nature of brain deformation during neurosurgery [44]. So far, most of the studies have focused on the registration of intra-operative US with pre-operative MR algorithms. Major findings reported by Reinertsen et. al. [45], Chen et. al. [46], and Farnia et. Al. [47] via feature-based registration methods. However, extraction of the corresponding features in two different modalities is an issue that directly affects the accuracy of these methods. In the intensity-based area, the different nature of US and MRI contrast mechanisms leads to failure of the common similarity measures such as mutual information [48,49]. However, effective solutions have been proposed by Wein et. al. [50], Coupé et. al. [51], Rivas et. al. [52,53], and Machado et. al. [54] for multimodal image registration which face different limitations.

Recently, multimodal image registration based on sparse representation of images has attracted enormous interest. The main idea of image registration based on sparse representation lies in the fact that different images can be represented as a combination of a few atoms in an over-complete dictionary [55]. Therefore, the sparse coefficients describe the salient features of the images. Generally, over-complete dictionaries can be constructed via two different approaches. In the first category, the standard fixed transform is applied as an over-complete dictionary. Fixed dictionaries such as discrete cosine transform, wavelet, and curvelet are used for multi-modal image registration [19,56,57]. Using fixed dictionaries benefits from simplicity and fast implementation. However, it is not customized for different types of data. In the second approach, an over-complete dictionary was constructed via learning methods. Among learning methods, the K-singular value decomposition (K-SVD) method has been widely used for image regis-

tration [58]. There are some studies which used synthesis sparse models for multimodal image registration [59]. However, a learned dictionary includes a large number of atoms. This leads to the increased computational complexity of multi-modal image registration, which is not suitable for real-time compensation of brain shift.

The analysis sparse model, named the co-sparse analysis model, represents a powerful alternative to the synthesis sparse representation approach in order to reduce the computational time [60]. Co-sparse analysis models can yield richer feature representations and better results for image registration in real-time processes. As a result of richer feature representation using co-sparse analysis models, a better results for image registration can be obtained in real-time processes [61,62]. There are a few studies for multi-modal image registration via a co-sparse analysis model, and none of them were in the medical field. Kiechle et. al. proposed an analysis model in a joint co-sparsity setup for different modalities of depth and intensity images [63]. Chang Han et. al. utilized the analysis sparse model for remote sensing images [64] and Gao et. al. used it to register multi-focus noisy images with higher quality images [65]. In our previous work, we could apply an analysis sparse model for US-MR image registration to compensate for the brain shift [66].

To date, a few research studies have investigated PA and MR image registration. Ren et. al. proposed a PA-MR image registration method based on mutual information to yield more insights into physiology and pathophysiology [67]. Gehrung et. al. proposed co-registration of PA and MR images of murine tumor models for assessment of tumor physiology [68]. However, these studies were dedicated to solve the rigid registration problems and also did not focus on the intra-operative application of PA imaging, and therefore did not face any complicated brain deformation.

To the best of our knowledge, in this study for the first time, PA and MR image registration was used for the purpose of compensating complicated brain shift phenomena. The co-sparse analysis model is proposed for PA-MR image registration which is able to capture the interdependency of two modalities. The algorithm works based on the minimization of mapping transform by using a pair of analysis operators which are learned by the alternating direction method of multipliers (ADMM).

2. Materials and Methods

2.1. Brain-mimicking phantom data

To assess the performance of the multi-modal image registration algorithm to compensate for brain shift, a phantom that mimics brain tissue was prepared. The phantom was made of Polyvinyl Alcohol Cryogel (PVA-C) which has been successfully used for mimicking brain tissue in previous studies [19]. The PVA-C material also has been applied in the fabrication of phantoms for ultrasound, MRI, and recently PA imaging [69]. A 10% by weight PVA in water solution was used to form PVA-C, which is solidified through a freeze-thaw process. The dimensions of the phantom were approximately 150 × 40 mm, with a curved top surface mimicking the shape of a head as shown in Figure 1 (a). Two plastic tubes with 1.2 and 1.4 mm inside diameters were inserted randomly into the mold before the freeze-thaw cycle to simulate blood vessels. Figure 1 (b) shows the 3D model of the phantom including random vessels. Two types of chromophores, copper sulfate pentahydrate ($CuSO_4(H_2O)_5$) and human blood (1:100 dilution); were used to fill embedded vessels before PA imaging (Figure 1 (c)).

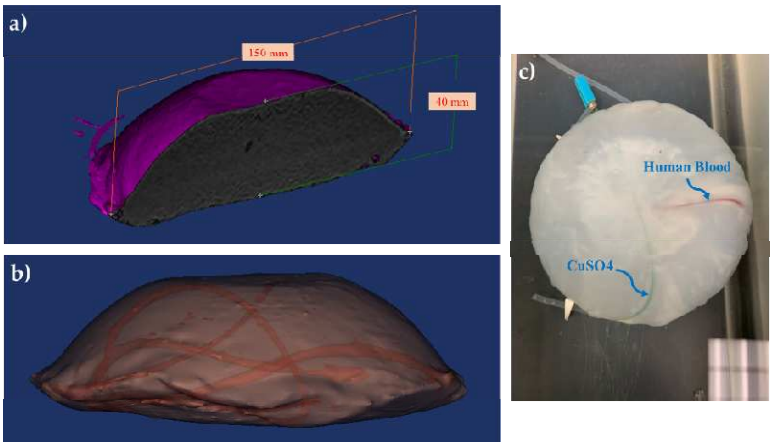

Figure 1. Brain-mimicking phantom design and fabrication (a) The dimensions of the phantom were about 150 × 40 mm, (b) a 3D model of the phantom including two simulated vessels with 1.2 and 1.4 mm inside diameters were inserted randomly to the phantom, (c) The cross-section of the phantom with vessels are filled using two different contrast agents $CuSO_4$ $(H_2O)_5$ and human blood.

To acquire MR images of the phantom before any deformations, the phantom was scanned using a Siemens scanner 1.5 Tesla using a standard T1 and T2 weighted protocol. Pulse-sequence parameters were set to TR=600 ms, TE=10 ms, Ec=1/1 27.8 kHz for T1 weighted and TR=8.6, TE=3.2, TI=450, Ec=1/1 31.3 kHz for T2 weighted considering 1mm slice thickness with full brain phantom coverage and 1 mm isotropic resolution.

PA images were achieved by using an ultrasound scanner (Vantage 128, Verasonics Inc., Kirkland, WA, USA) with a 128-element linear array US transducer (L11-4v, Verasonics, Inc., Kirkland, WA, USA) operating at a frequency range between 4 to 9 MHz. A pulsed tunable laser (PhocusCore, Optotek, California, USA) and Nd:YAG/OPO nanosecond pulsed laser (Phocus core system, OPOTEK Inc., USA), with the pulse repetition rate of 10 Hz at wavelengths of 700, 800, and 900 nm were used to illuminate the phantom. The scan resolution was 1 mm, and the laser fluence was ~1 mJ/cm2 (Figure 2).

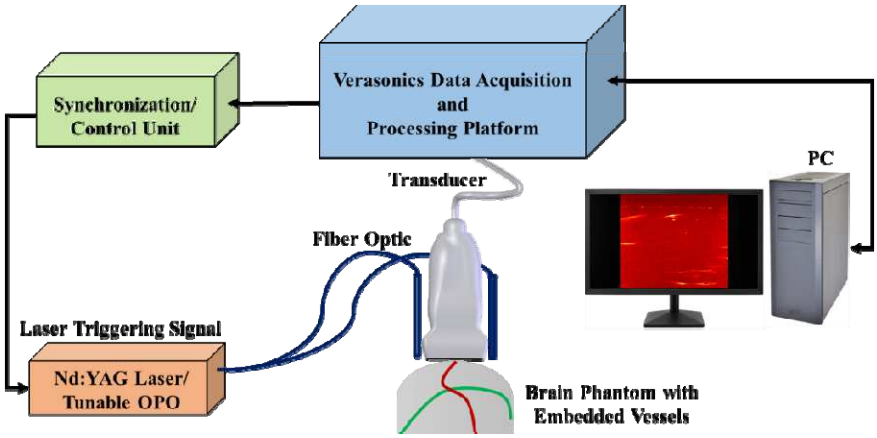

Figure 2. Schematic of the PA imaging setup, which includes a tunable pulsed laser and a programmable ultrasound data acquisition system.

2.2. Murine brain data

For further evaluation of the proposed image registration method, we used *ex-vivo* mouse brain data which was provided by Ren. et. al. in a previous study [67]. After removal of the mouse brain skull, the whole brain of mouse was embedded in agar 3% in

phosphate-buffered saline and then was imaged *ex-vivo*. To acquire T_2-weighted MR images of the mouse brain, a 2-D spin-echo sequence with imaging parameters of TR=2627.7 ms, TE=36 ms, slice thickness of 0.7 mm, a field of view of 20 ×20 mm, and scanning time of 12.36 min were used. For PA imaging, the laser excitation pulses of 9 ns were delivered at five wavelengths (680, 715, 730, 760, 800, and 850 nm) in coronal orientation with a field of view of 20 ×20 mm, step sizes of 0.3 mm moving along horizontal direction, and scan time of 20 minutes. To validate these data, five natural anatomical landmarks were manually selected as registration targets (Figure 3).

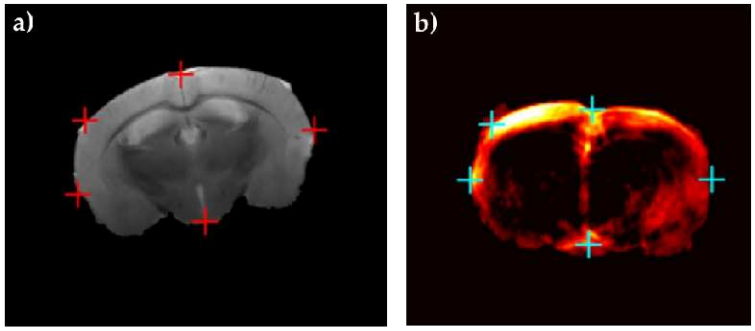

Figure 3. Ex-vivo head of mouse data (a) MR image, (b) PA image, five registration targets are shown in red and blue markers in (a) and (b) respectively, to assess the performance of the registration algorithm [67].

2.3. Inducing Brain Deformation

The proposed algorithm was designed to compensate for brain deformation during neurosurgery. Since the brain deformation is a complicated non-linear transformation, it is a challenging task to implement it physically on the phantom or mouse brain data. To evaluate our proposed registration algorithm, we performed brain deformation numerically by applying pre-defined pixel shifts to images. For this purpose, we used pre-operative and intra-operative MR images of brain tissue. The intra-operative MR image was considered as a gold standard. The deformation matrix was obtained by mono-modal registration of these images using the residual complexity algorithm [70] (Figure 4). Then the obtained brain deformation matrix was applied on PA images of brain phantom and mouse brain data.

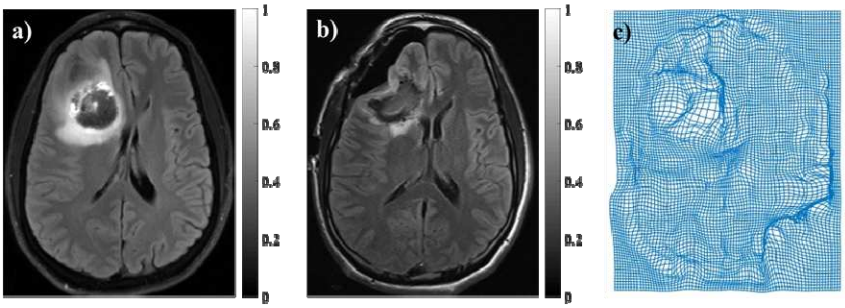

Figure 4. (a) Pre-operative MR image, (b) Intra-operative MR image, (c) Brain deformation filed was achieved by registration of intra-operative and pre-operative MR images using residual complexity method.

2.4. PA-MR Image Registration Framework

The workflow for automatic multi-modal image registration to compensate for the brain deformation was shown in Figure 5. After preparing two data sets, including brain-mimicking phantom data and murine brain data, pre-deformation MR images were

set as reference images, and pre-deformation PA images were set as float images. Then a real brain deformation matrix which was achieved by registration of intra-operative and pre-operative patient MR images using the residual complexity method was applied on PA images to generate deformed PA images. Then, by using the proposed registration method based on joint co-sparse analysis, registration of the MR image and deformed PA image was done. Finally, image registration results were evaluated and visualized for brain shift calculation. To evaluate the registration algorithm, root mean square error (RMSE) was calculated for phantom and mouse image registration. Additionally, target registration error (TRE) was calculated for defined targets in phantom and mouse brain data. Furthermore, we used the Hausdorff Distance (HD) between the PA and MR images. The HD between two point sets is defined as:

$$HD(I_{PA}, I_{MR}) = Max\ [Max\ Min\ d(I_{PA}, I_{MR}),\ Min\ Max\ d(I_{PA}, I_{MR})]$$

where, $d(.,.)$ is the Euclidean distance between the locations, and a smaller value of HD indicates a better alignment of the boundaries. To avoid the effect of outliers [73], we used 95% HD instead of maximum HD.

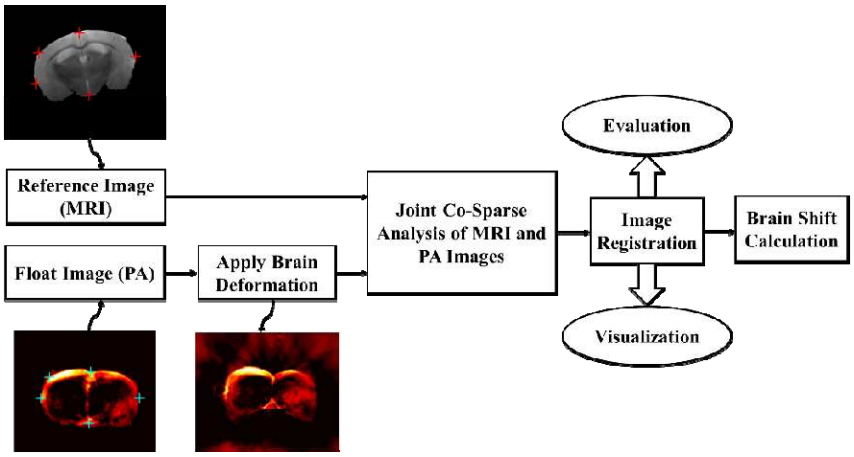

Figure 5. The workflow for automatic multi-modal image registration to compensate for brain deformation. MR and PA images including pre-defined targets were set as a reference and float images, respectively. After applying brain deformation on PA images, registration of MR and deformed PA was done and evaluated.

2.5. Co-sparse analysis model

Image (I) can be approximated via the sparse representation $x \in R^n$ which is a linear combination of a few non-zero elements (named atoms) in an over-complete dictionary matrix $D \in R^{n \times k}$ ($n << k$).

$$x \approx D\alpha \quad (1)$$

where $\alpha \in R^k$ is a sparse vector with the fewest k non-zero elements. The sparse coefficients describe the salient features of the images. Therefore, the sparse representation problem could be solved as the following optimization problem:

$$\min_{\alpha} \|\alpha\|_0, s.t \|x - D\alpha\|_2 \leq \varepsilon \quad (2)$$

Here, $\|\alpha\|_0$ is the zero norm of α that represents the number of non-zero values in a vector (α). The sparse representation of an image considers that a synthesis dictionary represents the redundant signals.

There is also another representation of image based on the co-sparse analysis model [60]. This alternative assumes that for a signal of interest (x), there exists an analysis operator $\Omega \in R^{k \times n}$ such that $\Omega x \approx \alpha$ as an analyzed vector is sparse for all $x \in R^n$. The rows of Ω represent filters that provide sparse responses and indices of the filters with zero response determine the subspace to which the signal belongs to. This subspace is the intersection of all hyperplanes to which these filters are normal vectors, and therefore, the information of signals is encoded in its zero responses. The index set of the zero entries of Ωx is called the *co-support* of x as below:

$$\cos upp(\Omega x) := \left\{ j \mid (\Omega x)_j = 0 \right\} \tag{3}$$

As the key property of analysis sparse models, these models put an emphasis on the zeros in the analysis representation rather than the non-zeros in the sparse representation of the signal. These zeros in the analysis representation model inscribe the low-dimensional subspace which the signal belongs to. Consequently, analysis operator learning procedures finds the suitable operator Ω for signal X as below:

$$\Omega^* \in \arg\min \sum_i \left\| \Omega x_i \right\|_0 \tag{4}$$

Where Ω^* is the optimized operator Ω. In order to relax the co-sparsity assumption, the log-square function as a proper approximation of zero norm is used for large values of ν as below:

$$g(\alpha) := \sum_k \log(1 + \nu \alpha_k^{\ 2}) \tag{5}$$

where ν is the positive weight. Therefore, equation (4) could be converted to:

$$\Omega^* \in \arg\min \sum_i g(\Omega x_i) \tag{6}$$

One should consider that there has been three main constraints on the Ω^* to avoid trivial solutions as below [71]:

1. The rows of Ω^* have unit Euclidean norm; $\Omega^* \in oblique \quad manifold$.
2. The operator Ω^* has full rank, i.e., it has the maximal number of linear independent rows.

$$h(\Omega^*) = -\frac{1}{n \log(n)} \log \det\left(\frac{1}{m} \Omega^{*T} \Omega^*\right),$$

3. The rows of the operator Ω^* are not trivially linearly dependent.

$$r(\Omega^*) = -\sum_{k<1} \log(1 - (\Omega_k^{\ T} \Omega_l)^2) \tag{7}$$

2.6. Multi-modal Image registration algorithm

In this study, we formulated the multimodal image registration problem in terms of an analysis co-sparse model. There are different co-sparse models that could be used in multimodal image registration approaches [72]. In our approach, a joint analysis co-sparse model (JACSM) was proposed for the registration of PA and MR images. JACSM indicates that different signals from different sensors of the same scene form an ensemble. The signals in an ensemble include a common sparse component, shared between all of them, and an innovation component which represents individual differences [73].

Consider two images I_{PA} and I_{MR} which are provided through PA and MR imaging, respectively, from a brain simulated phantom as the input data. The interdepend-

ency of the two image modalities was modeled via JACSM and common sparse components were considered in this study. This image pair has a co-sparse representation with an appropriate pair of analysis operators $(\Omega_{PA}, \Omega_{MR}) \in R^{k\times n_{PA}} \times R^{k\times n_{MR}}$. By considering the structures of images encoded in their co-supports based on equation (3), there is a pair of analysis operators so that the intersection of the co-supports of $\Omega_{PA} I_{PA}$ and $\Omega_{MR} I_{MR}$ is large. In particular, we try to learn the pair of co-sparse analysis operators $(\Omega_{PA}, \Omega_{MR})$ for two different image modalities.

On the other hand, the PA and MR images should be matched with a transformation T such that:

$$I_{MR}(Tx) \approx I_{PA}(x), \qquad for\ all\ \ pixel\ \ cordinate\ \ x \tag{8}$$

which x determines homogeneous pixel coordinates in PA images. The goal of multi-modal image registration problem in this approach is to optimize T by using the pair of analysis operators $(\Omega_{PA}, \Omega_{MR})$. We consider that for an optimized transformation, there is a coupled sparsity measure to be minimized. Thus, by considering equation (6) and constraints based on equation (7), we are searching for T^* such that:

$$\begin{aligned} T^* \in \arg\min \frac{1}{N}\sum_{i=1}^{N} g(\Omega_{PA} {I_{PA}}^{(i)}, \Omega_{MR} I_{MR}(Tx)^{(i)}) - \\ k\ \frac{1}{n\log(n)}[\log\det(\frac{1}{m}{\Omega_{MR}}^{*^T}\Omega_{MR}^{*}) + \log\det(\frac{1}{m}{\Omega_{PA}}^{*^T}\Omega_{PA}^{*})] - \\ \mu\sum_{r<1}\log(1-(\Omega_{PAr}{}^T\Omega_{PAl})^2) + \log(1-(\Omega_{MRr}{}^T\Omega_{MRl})^2). \end{aligned} \tag{9}$$

To tackle the problem of equation (9), we propose the ADMM. In other words, the analysis operators were learned by optimizing a JACSM via an ADMM. The ADMM as a candidate solver for convex problems, breaking our main problem into smaller sub-problems as below:

$$\min f(x) + g(y), \quad s.t.\ Ax + By = c \tag{10}$$

where $x \in R^n$, $y \in R^m$, $A \in R^{p\times n}$, and $B \in R^{p\times m}$. The augmentation Lagrangian for the equation (10) can be written as:

$$L_p(x, y, \lambda) = f(x) + g(y) + \lambda^T(Ax + By - c) + (\frac{\rho}{2})\|Ax + By - c\|_2^2 \tag{11}$$

where the term ρ is a penalty term that is considered positive and λ is the Lagrangian multiplier. Equation (11) is solved over three steps: x-minimization, and y-minimization, these two are split into N separate problems and followed by an updating step for the multiplier λ as follows:

$$\begin{aligned} x^{k+1} &:= \arg\min_x L_p(x, y^k, \lambda^k), \\ y^{k+1} &:= \arg\min_y L_p(x^{k+1}, y, \lambda^k), \\ \lambda^{k+1} &:= \lambda^k + \rho(Ax^{k+1} + By^{k+1} - c). \end{aligned} \tag{12}$$

3. Results & Discussion

To implement the proposed image registration algorithm, a total of 20000 pairs of square sample patches of size 7 pixels from the total of images in the training set were randomly selected. It is notable that in our experiments, the patch sizes 3, 5, 7, 9, and 11 pixels were applied. Based on our experience, a small patch size would cause an over smooth effect, and a larger patch size would lead to more computation. Therefore, based on our results, the patch size of 7×7 was selected to balance the two effects.

The performance of the JACSM-based registration method was evaluated using a phantom with simulated vessels and using ex-vivo mouse brain data with anatomical landmarks. In Figure 6, the performance of the proposed registration method for PA-MR, US-MR, and MR-MR images on the phantom data were shown and compared. In the first row, the MR image and its corresponding US and PA images were shown. Dashed yellow circles show the same fields of view in three different modalities (MRI, US, and PA). Corresponding structures which are used to calculate target registration error are labeled with numbers 1 to 3 in the three imaging modalities. The brain deformation field is applied to the images in the first row, and the second row represents deformed MR, US, and PA images. As shown in Figure 6 (d), (e), and (f), labeled targets have been displaced due to inducing deformation. Finally, the images in the third row show the image registration results of MR, US, and PA after deformation (second row) with the original MRI before deformation (Figure 6 (a)). The result of registration between the original MR image and deformed MR image (Figure 6 (g)) is used as a gold standard to evaluate the proposed algorithm. Also, the registration result of the deformed PA image (Figure 6 (i)) is compared to the registration result of deformed ultrasound image (Figure 6 (h)) as a commonly used intra-operative imaging modality for brain shift compensation. As we have shown in the third row, images registered more accurate in MR-MR images registration compared to PA-MR image registration. Also, images registered more accurately in PA-MR image registration compared to the US-MR image registration. As we have shown with the blue arrow in the third-row images, the surface of the phantom is matched accurately in the result of MR-MR image registration. It is while, registration of US-MR has the worst performance in matching the surface of the phantom in two modalities, and registration of PA-MR has an acceptable performance in matching the surface of the phantom in two modalities, PA and MRI.

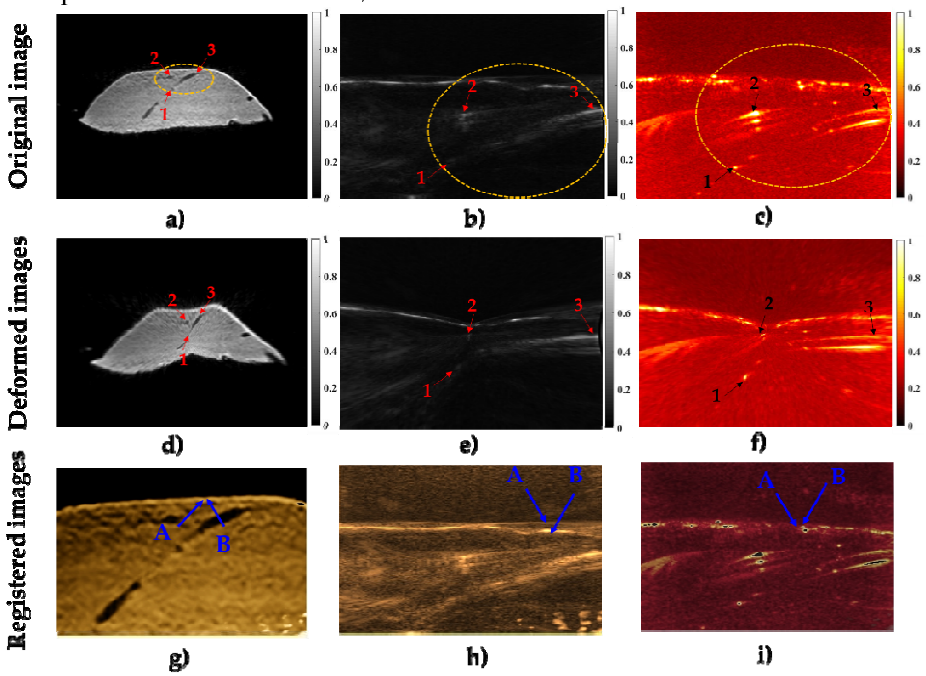

Figure 6. The results of multi-modal image registration of phantom data. First row: Original image of phantom data before deformation from three different modalities (a) MRI, (b) US, and (c) PA, second row: Deformed images of (d) MRI, (e) US, and (f) PA. The third row shows the results of registered images of (g) MR-MR, (f) US-MR, and (g) PA-MR. The blue arrows in third row represent the surface of the phantom in different modalities. Blue arrows A are related to the surface of the phantom in original MR images and blue arrows B are related to the surface of the phantom in deformed MR, deformed US, and deformed PA images, in (g), (h), and (i), respectively.

To quantitative evaluation of the proposed registration method, RMSE, TRE, and HD for PA-MR, US-MR, and MR-MR image registration were calculated and shown in Table.1. Also, for further evaluation the results of our proposed method were compared to the commonly used normalized mutual information (NMI) registration method. In total, we used 23 phantom data. Registration accuracy of MR and MR images was considered as a gold standard. Also, the algorithms are implemented in MATLAB, and tested on an Intel Corei7 3.2 GHz CPU with 8GB RAM.

Table 1. Evaluation of proposed registration methods on phantom data.

Multimodal Registration		RMSE (mean±std)	TRE (mean±std) Number of targets: 3	HD (mean±std)
MR-MR	JACSM	0.62±0.04	0.32±0.03	0.21±0.03
	NMI	0.98±0.09	0.51±0.04	0.46±0.07
US-MR	JACSM	1.17±0.13	0.96±0.08	0.51±0.03
	NMI	1.87±0.15	1.58±0.11	1.23±0.13
PA-MR	JACSM	0.73±0.05	0.58±0.04	0.32±0.04
	NMI	1.18±0.09	0.96±0.08	0.68±0.05

The results of the phantom study showed that PA-MR image registration has better RMSE, TRE, and HD about 60%, 65%, and 59% compared to US-MR image registration as a common imaging modality for brain shift compensation, respectively. On the other hand, the proposed method reached an RMSE of about 0.73 mm which is acceptable in comparison with MR-MR image registration as a gold standard with an RMSE of about 0.62 mm. The proposed method improved the results of RMSE and TRE of about 60% and 63% (on average) compared to NMI.

For further evaluation of the proposed method, ex-vivo mouse brain data was used. In Figure 7, the performance of the JACSM-based registration method for PA-MR image registration for mouse brain data was shown and compared with MR-MR image registration. Figure 7 (a) and (b) represent MR and PA images of the mouse brain before any deformation, respectively. The PA image after applying non-linear deformation is shown in Figure 7 (c), and the registration result of deformed PA and original MR of mouse brain images is shown in Figure 7 (d). Also, in panel (e), the mean of RMSE, TRE, and HD of PA-MR image registration for all data of the mouse brain was calculated and compared to the result of MR-MR image registration.

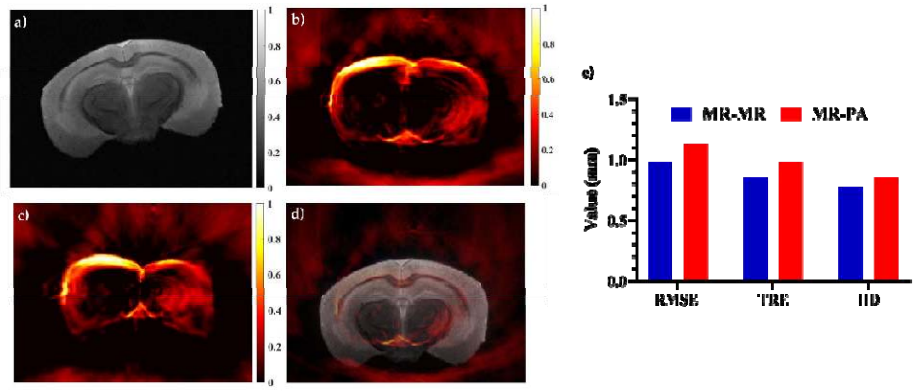

Figure 7. The results of multi-modal image registration of mouse brain data. (a) MRI, (b) PA image, (c) PA image after applying non-linear deformation, and (d) registration of deformed PA and MRI of mouse data. Panel (e) shows the mean of RMSE, TRE, and HD of PA-MR image registration for all data of the mouse brain.

The results acquired from the ex-vivo mouse brain also proved the ability of the proposed registration method to recover non-linear deformation with calculated mean of RMSE, TRE, and HD of 1.13, 0.98, and 0.85 mm, respectively. The results are acceptable when compared to the results of MRI-MRI registration as a gold standard, with RMSE, TRE, and HD of about 0.98, 0.85, and 0.77 mm. In fact, intra-operative PA imaging as a real-time imaging with about 15% RMSE increase, could be a good alternative to intra-operative MR imaging. Additionally, with a 60% improvement in registration accuracy, PA imaging could be an alternative for intra-operative ultrasound imaging.

Having a closer look at the comparison between synthesis and analysis models, the synthesis model contains very few low-dimensional subspaces and an increasingly large number of subspaces of higher dimension. In contrast, the analysis model includes a combinatorial number of low-dimensional subspaces with fewer high-dimensional subspaces. The co-sparse analysis models can yield richer feature representations, and joint co-sparse analysis models consider the common sparse components of different signals from different sensors. Therefore, the JACSM-based registration method was found to be more suitable for multi-modal image registration.

4. Conclusions

There has been a growing interest in intra-operative imaging approaches to update the pre-operative images with real-time data when tissue deformation occurs during surgery. In particular, accurate and real-time brain shift compensation remains a challenging problem during neurosurgery. For the first time in this study, we proposed the application of PA imaging as an interventional solution during neurosurgery in combination with pre-operative modalities such as MRI to track brain deformation. However, the accurate combination of PA and MR images requires the development of a real-time and robust image registration algorithm. Accurate registration of intra-operative PA images with pre-operative MR images of brain tissue could calculate and compensate for brain deformation. In this study, the JACSM based registration is proposed for PA-MR image registration which can capture the interdependency of two modalities. The proposed algorithm works based on the minimization of mapping transform by using a pair of analysis operators in PA and MR images which are learned by the ADMM. The algorithm was tested on two data sets of phantom and mouse brain data and the results showed more accurate performance for PA imaging versus US imaging for brain shift calculation. Furthermore, the proposed method showed about a 60% improvement in TRE in comparison with the common NMI registration method. The co-sparse analysis models can yield richer feature representations and better accuracy for medical image registration in the real-time process, which is crucial for surgeons during neurosurgery to compensate for brain shift. Finally, by using this JACSM-based registration, the intra-operative PA images could become a promising tool when the brain shift invalidated pre-operative MRI.

Author Contributions: Authors have made a group effort for this research. The conceptualization and study design were done by P.F and B.M. The methodology and algorithm were implemented by P. F under supervision of B. M. The phantom was designed and made by E. N under supervision of M. A. MR images was provided by E. N. The PA and ultrasound data was provided by M.B and Y.Y under the supervision of M.M. P.F and E. N wrote original draft and revised by M. M. and A.A. All the works done under supervision of A.A.

Funding: This research received no external funding.

Institutional Review Board Statement: Not applicable.

Informed Consent Statement: Not applicable.

Acknowledgments: The authors gratefully acknowledge the Dr. Ruiqing Ni from University of Zurich and ETH Zurich for providing mouse brain data.

Conflicts of Interest: The authors declare no conflict of interest.

References

1. D. A. Orringer, A. Golby, and F. J. E. r. o. m. d. Jolesz, "Neuronavigation in the surgical management of brain tumors: current and future trends," vol. 9, no. 5, pp. 491-500, 2012.
2. I. J. Gerard, M. Kersten-Oertel, K. Petrecca, D. Sirhan, J. A. Hall, and D. L. Collins, "Brain shift in neuronavigation of brain tumors: A review," Medical image analysis, vol. 35, pp. 403-420, 2017.
3. Y. Xiao, H. Rivaz, M. Chabanas, M. Fortin, I. Machado, Y. Ou, M. P. Heinrich, J. A. Schnabel, X. Zhong, and A. Maier, "Evaluation of MRI to ultrasound registration methods for brain shift correction: The CuRIOUS2018 Challenge," IEEE Transactions on Medical Imaging, 2019.
4. I. J. Gerard, M. Kersten-Oertel, J. A. Hall, D. Sirhan, and D. L. J. F. i. O. Collins, "Brain Shift in Neuronavigation of Brain Tumors: An Updated Review of Intra-Operative Ultrasound Applications," vol. 10, pp. 3390, 2021.
5. T. Mitsui, M. Fujii, M. Tsuzaka, Y. Hayashi, Y. Asahina, and T. Wakabayashi, "Skin shift and its effect on navigation accuracy in image-guided neurosurgery," Radiological physics and technology, vol. 4, no. 1, pp. 37-42, 2011.
6. D. L. Hill, C. R. Maurer, R. J. Maciunas, R. J. Maciunas, J. A. Barwise, J. M. Fitzpatrick, and M. Y. Wang, "Measurement of intraoperative brain surface deformation under a craniotomy," Neurosurgery, vol. 43, no. 3, pp. 514-526, 1998.
7. M. A. Hammoud, B. L. Ligon, R. Elsouki, W. M. Shi, D. F. Schomer, and R. Sawaya, "Use of intraoperative ultrasound for localizing tumors and determining the extent of resection: a comparative study with magnetic resonance imaging," Journal of neurosurgery, vol. 84, no. 5, pp. 737-741, 1996.
8. O. Škrinjar, A. Nabavi, and J. J. M. i. a. Duncan, "Model-driven brain shift compensation," vol. 6, no. 4, pp. 361-373, 2002.
9. A. Wittek, R. Kikinis, S. K. Warfield, and K. Miller, "Brain shift computation using a fully nonlinear biomechanical model." pp. 583-590.
10. M. I. Miga, K. Sun, I. Chen, L. W. Clements, T. S. Pheiffer, A. L. Simpson, R. C. J. I. j. o. c. a. r. Thompson, and surgery, "Clinical evaluation of a model-updated image-guidance approach to brain shift compensation: experience in 16 cases," vol. 11, no. 8, pp. 1467-1474, 2016.
11. P. Grunert, W. Müller-Forell, K. Darabi, R. Reisch, C. Busert, N. Hopf, and A. J. C. A. S. Perneczky, "Basic principles and clinical applications of neuronavigation and intraoperative computed tomography," vol. 3, no. 4, pp. 166-173, 1998.
12. C. Nimsky, O. Ganslandt, S. Cerny, P. Hastreiter, G. Greiner, and R. J. N. Fahlbusch, "Quantification of, visualization of, and compensation for brain shift using intraoperative magnetic resonance imaging," vol. 47, no. 5, pp. 1070-1080, 2000.
13. D. Kuhnt, M. H. Bauer, and C. J. C. R. i. B. E. Nimsky, "Brain shift compensation and neurosurgical image fusion using intraoperative MRI: current status and future challenges," vol. 40, no. 3, 2012.
14. O. Clatz, H. Delingette, I.-F. Talos, A. J. Golby, R. Kikinis, F. A. Jolesz, N. Ayache, and S. K. Warfield, "Robust nonrigid registration to capture brain shift from intraoperative MRI," IEEE transactions on medical imaging, vol. 24, no. 11, pp. 1417-1427, 2005.
15. P. A. Valdés, X. Fan, S. Ji, B. T. Harris, K. D. Paulsen, D. W. J. S. Roberts, and f. neurosurgery, "Estimation of brain deformation for volumetric image updating in protoporphyrin IX fluorescence-guided resection," vol. 88, no. 1, pp. 1-10, 2010.
16. J. W. Trobaugh, W. D. Richard, K. R. Smith, and R. D. Bucholz, "Frameless stereotactic ultrasonography: method and applications," Computerized Medical Imaging and Graphics, vol. 18, no. 4, pp. 235-246, 1994.
17. A. Roche, X. Pennec, M. Rudolph, D. Auer, G. Malandain, S. Ourselin, L. M. Auer, and N. Ayache, "Generalized correlation ratio for rigid registration of 3D ultrasound with MR images." pp. 567-577.
18. J. Koivukangas, J. Ylitalo, E. Alasaarela, and A. Tauriainen, "Three-dimensional ultrasound imaging of brain for neurosurgery," Annals of clinical research, vol. 18, pp. 65-72, 1986.
19. P. Farnia, A. Ahmadian, T. Shabanian, N. D. Serej, and J. Alirezaie, "Brain-shift compensation by non-rigid registration of intra-operative ultrasound images with preoperative MR images based on residual complexity," International journal of computer assisted radiology and surgery, vol. 10, no. 5, pp. 555-562, 2015.
20. S. Bayer, A. Maier, M. Ostermeier, and R. J. I. j. o. b. i. Fahrig, "Intraoperative imaging modalities and compensation for brain shift in tumor resection surgery," vol. 2017, 2017.
21. P. Farnia, M. Mohammadi, E. Najafzadeh, M. Alimohamadi, B. Makkiabadi, and A. Ahmadian, "High-quality photoacoustic image reconstruction based on deep convolutional neural network: towards intra-operative photoacoustic imaging," Biomedical Physics & Engineering Express, 2020.
22. M. Pramanik, G. Ku, C. Li, and L. V. Wang, "Design and evaluation of a novel breast cancer detection system combining both thermoacoustic (TA) and photoacoustic (PA) tomography," Medical physics, vol. 35, no. 6Part1, pp. 2218-2223, 2008.
23. M. Mehrmohammadi, S. Joon Yoon, D. Yeager, and S. J. C. M. I. Y Emelianov, "Photoacoustic imaging for cancer detection and staging," vol. 2, no. 1, pp. 89-105, 2013.
24. E. Najafzadeh, H. Ghadiri, M. Alimohamadi, P. Farnia, M. Mehrmohammadi, and A. Ahmadian, "Application of multi-wavelength technique for photoacoustic imaging to delineate tumor margins during maximum-safe resection of glioma: A preliminary simulation study," Journal of Clinical Neuroscience, 2019.

25. S. Arabpou, E. Najafzadeh, P. Farnia, A. Ahmadian, H. Ghadiri, and M. S. A. Akhoundi, "Detection of Early Stages Dental Caries Using Photoacoustic Signals: The Simulation Study," Frontiers in Biomedical Technologies, 2019.
26. C. Moore, Y. Bai, A. Hariri, J. B. Sanchez, C.-Y. Lin, S. Koka, P. Sedghizadeh, C. Chen, and J. V. Jokerst, "Photoacoustic imaging for monitoring periodontal health: A first human study," Photoacoustics, vol. 12, pp. 67-74, 2018.
27. Y. Yan, S. John, M. Ghalehnovi, L. Kabbani, N. A. Kennedy, and M. J. S. r. Mehrmohammadi, "photoacoustic Imaging for Image-guided endovenous Laser Ablation procedures," vol. 9, no. 1, pp. 1-10, 2019.
28. E. Petrova, H. Brecht, M. Motamedi, A. Oraevsky, S. J. P. i. M. Ermilov, and Biology, "In vivo optoacoustic temperature imaging for image-guided cryotherapy of prostate cancer," vol. 63, no. 6, pp. 064002, 2018.
29. B. Eddins, and M. A. L. J. J. o. b. o. Bell, "Design of a multifiber light delivery system for photoacoustic-guided surgery," vol. 22, no. 4, pp. 041011, 2017.
30. L. V. Wang, and S. Hu, "Photoacoustic tomography: in vivo imaging from organelles to organs," science, vol. 335, no. 6075, pp. 1458-1462, 2012.
31. L. V. Wang, and J. Yao, "A practical guide to photoacoustic tomography in the life sciences," Nature methods, vol. 13, no. 8, pp. 627, 2016.
32. A. B. E. Attia, G. Balasundaram, M. Moothanchery, U. Dinish, R. Bi, V. Ntziachristos, and M. Olivo, "A review of clinical photoacoustic imaging: Current and future trends," Photoacoustics, pp. 100144, 2019.
33. P. Beard, "Biomedical photoacoustic imaging," Interface focus, vol. 1, no. 4, pp. 602-631, 2011.
34. A. Rosencwaig, and A. Gersho, "Theory of the photoacoustic effect with solids," Journal of Applied Physics, vol. 47, no. 1, pp. 64-69, 1976.
35. S. Zackrisson, S. Van De Ven, and S. Gambhir, "Light in and sound out: emerging translational strategies for photoacoustic imaging," Cancer research, vol. 74, no. 4, pp. 979-1004, 2014.
36. [36] M. Xu, and L. V. Wang, "Photoacoustic imaging in biomedicine," Review of scientific instruments, vol. 77, no. 4, pp. 041101, 2006.
37. P. Farnia, E. Najafzadeh, A. Hariri, S. N. Lavasani, B. Makkiabadi, A. Ahmadian, and J. V. Jokerst, "Dictionary learning technique enhances signal in LED-based photoacoustic imaging," Biomedical Optics Express, vol. 11, no. 5, pp. 2533-2547, 2020.
38. C. Hoelen, F. De Mul, R. Pongers, and A. Dekker, "Three-dimensional photoacoustic imaging of blood vessels in tissue," Optics letters, vol. 23, no. 8, pp. 648-650, 1998.
39. P. Raumonen, and T. Tarvainen, "Segmentation of vessel structures from photoacoustic images with reliability assessment," Biomedical optics express, vol. 9, no. 7, pp. 2887-2904, 2018.
40. E. Najafzadeh, H. Ghadiri, M. Alimohamadi, P. Farnia, M. Mehrmohammadi, and A. Ahmadian, "Evaluation of multi-wavelengths LED-based photoacoustic imaging for maximum safe resection of glioma: a proof of concept study," International Journal of Computer Assisted Radiology and Surgery, 2020.
41. M. S. Karthikesh, X. J. E. B. Yang, and Medicine, "Photoacoustic image-guided interventions," vol. 245, no. 4, pp. 330-341, 2020.
42. S. H. J. N. Han, "Review of photoacoustic imaging for imaging-guided spinal surgery," vol. 15, no. 4, pp. 306, 2018.
43. K. P. Kubelick, S. Y. J. U. i. M. Emelianov, and Biology, "A Trimodal Ultrasound, Photoacoustic and Magnetic Resonance Imaging Approach for Longitudinal Post-operative Monitoring of Stem Cells in the Spinal Cord," vol. 46, no. 12, pp. 3468-3474, 2020.
44. D. H. Iversen, W. Wein, F. Lindseth, G. Unsgård, and I. Reinertsen, "Automatic intraoperative correction of brain shift for accurate neuronavigation," World neurosurgery, vol. 120, pp. e1071-e1078, 2018.
45. I. Reinertsen, M. Descoteaux, K. Siddiqi, and D. L. Collins, "Validation of vessel-based registration for correction of brain shift," Medical image analysis, vol. 11, no. 4, pp. 374-388, 2007.
46. S. J.-S. Chen, I. Reinertsen, P. Coupé, C. X. Yan, L. Mercier, D. R. Del Maestro, and D. L. Collins, "Validation of a hybrid Doppler ultrasound vessel-based registration algorithm for neurosurgery," International journal of computer assisted radiology and surgery, vol. 7, no. 5, pp. 667-685, 2012.
47. P. Farnia, A. Ahmadian, A. Khoshnevisan, A. Jaberzadeh, N. D. Serej, and A. F. Kazerooni, "An efficient point based registration of intra-operative ultrasound images with MR images for computation of brain shift; A phantom study." pp. 8074-8077.
48. T. Arbel, X. Morandi, R. M. Comeau, and D. L. Collins, "Automatic non-linear MRI-ultrasound registration for the correction of intra-operative brain deformations." pp. 913-922.
49. S. Ji, A. Hartov, D. Roberts, and K. Paulsen, "Mutual-information-corrected tumor displacement using intraoperative ultrasound for brain shift compensation in image-guided neurosurgery." p. 69182H.
50. W. Wein, A. Ladikos, B. Fuerst, A. Shah, K. Sharma, and N. Navab, "Global registration of ultrasound to MRI using the LC 2 metric for enabling neurosurgical guidance." pp. 34-41.
51. P. Coupé, P. Hellier, X. Morandi, and C. Barillot, "3D rigid registration of intraoperative ultrasound and preoperative MR brain images based on hyperechogenic structures," Journal of Biomedical Imaging, vol. 2012, pp. 1, 2012.
52. H. Rivaz, Z. Karimaghaloo, and D. L. Collins, "Self-similarity weighted mutual information: a new nonrigid image registration metric," Medical image analysis, vol. 18, no. 2, pp. 343-358, 2014.
53. H. Rivaz, S. J.-S. Chen, and D. L. Collins, "Automatic deformable MR-ultrasound registration for image-guided neurosurgery," IEEE transactions on medical imaging, vol. 34, no. 2, pp. 366-380, 2015.

54. I. Machado, M. Toews, E. George, P. Unadkat, W. Essayed, J. Luo, P. Teodoro, H. Carvalho, J. Martins, and P. Golland, "Deformable MRI-ultrasound registration using correlation-based attribute matching for brain shift correction: Accuracy and generality in multi-site data," NeuroImage, vol. 202, pp. 116094, 2019.
55. Q. Zhang, Y. Liu, R. S. Blum, J. Han, and D. Tao, "Sparse representation based multi-sensor image fusion for multi-focus and multi-modality images: A review," Information Fusion, vol. 40, pp. 57-75, 2018.
56. P. Farnia, A. Ahmadian, T. Shabanian, N. D. Serej, and J. Alirezaie, "A hybrid method for non-rigid registration of intra-operative ultrasound images with pre-operative MR images." pp. 5562-5565.
57. P. Farnia, B. Makkiabadi, A. Ahmadian, and J. Alirezaie, "Curvelet based residual complexity objective function for non-rigid registration of pre-operative MRI with intra-operative ultrasound images." pp. 1167-1170.
58. K. Huang, and S. Aviyente, "Sparse representation for signal classification." pp. 609-616.
59. A. Roozgard, N. Barzigar, P. Verma, and S. Cheng, "3D-SCoBeP: 3D medical image registration using sparse coding and belief propagation," International Journal of Diagnostic Imaging, vol. 2, no. 1, pp. 54, 2014.
60. S. Nam, M. E. Davies, M. Elad, and R. Gribonval, "The cosparse analysis model and algorithms," Applied and Computational Harmonic Analysis, vol. 34, no. 1, pp. 30-56, 2013.
61. N. Zhou, H. Jiang, L. Gong, and X. Xie, "Double-image compression and encryption algorithm based on co-sparse representation and random pixel exchanging," Optics and Lasers in Engineering, vol. 110, pp. 72-79, 2018.
62. M. Kiechle, S. Hawe, and M. Kleinsteuber, "A joint intensity and depth co-sparse analysis model for depth map super-resolution." pp. 1545-1552.
63. M. Kiechle, T. Habigt, S. Hawe, and M. Kleinsteuber, "A bimodal co-sparse analysis model for image processing," International Journal of Computer Vision, vol. 114, no. 2-3, pp. 233-247, 2015.
64. C. Han, H. Zhang, C. Gao, C. Jiang, N. Sang, and L. Zhang, "A Remote Sensing Image Fusion Method Based on the Analysis Sparse Model," IEEE Journal of Selected Topics in Applied Earth Observations and Remote Sensing, vol. 9, no. 1, pp. 439-453, 2016.
65. R. Gao, S. A. Vorobyov, and H. Zhao, "Image fusion with cosparse analysis operator," IEEE Signal Processing Letters, vol. 24, no. 7, pp. 943-947, 2017.
66. P. Farnia, E. Najafzadeh, A. Ahmadian, B. Makkiabadi, M. Alimohamadi, and J. Alirezaie, "Co-sparse analysis model based image registration to compensate brain shift by using intra-operative ultrasound imaging." pp. 1-4.
67. W. Ren, H. Skulason, F. Schlegel, M. Rudin, J. Klohs, and R. Ni, "Automated registration of magnetic resonance imaging and optoacoustic tomography data for experimental studies," Neurophotonics, vol. 6, no. 2, pp. 025001, 2019.
68. M. Gehrung, M. Tomaszewski, D. McIntyre, J. Disselhorst, and S. Bohndiek, "Co-Registration of Optoacoustic Tomography and Magnetic Resonance Imaging Data from Murine Tumour Models," Photoacoustics, pp. 100147, 2020.
69. K. Surry, H. Austin, A. Fenster, and T. Peters, "Poly (vinyl alcohol) cryogel phantoms for use in ultrasound and MR imaging," Physics in Medicine & Biology, vol. 49, no. 24, pp. 5529, 2004.
70. A. Myronenko, and X. Song, "Intensity-based image registration by minimizing residual complexity," IEEE transactions on medical imaging, vol. 29, no. 11, pp. 1882-1891, 2010.
71. S. Hawe, M. Kleinsteuber, and K. Diepold, "Analysis operator learning and its application to image reconstruction," IEEE Transactions on Image Processing, vol. 22, no. 6, pp. 2138-2150, 2013.
72. S. Cai, Z. Kang, M. Yang, X. Xiong, C. Peng, and M. J. S. Xiao, "Image denoising via improved dictionary learning with global structure and local similarity preservations," vol. 10, no. 5, pp. 167, 2018.
73. Q. Zhang, Y. Fu, H. Li, and J. Zou, "Dictionary learning method for joint sparse representation-based image fusion," Optical Engineering, vol. 52, no. 5, pp. 057006, 2013.

1. Orringer, D.A.; Golby, A.; Jolesz, F.J.E.r.o.m.d. Neuronavigation in the surgical management of brain tumors: current and future trends. **2012**, *9*, 491-500.
2. Gerard, I.J.; Kersten-Oertel, M.; Petrecca, K.; Sirhan, D.; Hall, J.A.; Collins, D.L. Brain shift in neuronavigation of brain tumors: A review. *Medical image analysis* **2017**, *35*, 403-420.
3. Xiao, Y.; Rivaz, H.; Chabanas, M.; Fortin, M.; Machado, I.; Ou, Y.; Heinrich, M.P.; Schnabel, J.A.; Zhong, X.; Maier, A. Evaluation of MRI to ultrasound registration methods for brain shift correction: The CuRIOUS2018 Challenge. *IEEE Transactions on Medical Imaging* **2019**.
4. Gerard, I.J.; Kersten-Oertel, M.; Hall, J.A.; Sirhan, D.; Collins, D.L.J.F.i.O. Brain Shift in Neuronavigation of Brain Tumors: An Updated Review of Intra-Operative Ultrasound Applications. **2021**, *10*, 3390.
5. Mitsui, T.; Fujii, M.; Tsuzaka, M.; Hayashi, Y.; Asahina, Y.; Wakabayashi, T. Skin shift and its effect on navigation accuracy in image-guided neurosurgery. *Radiological physics and technology* **2011**, *4*, 37-42.

6. Hill, D.L.; Maurer, C.R.; Maciunas, R.J.; Maciunas, R.J.; Barwise, J.A.; Fitzpatrick, J.M.; Wang, M.Y. Measurement of intraoperative brain surface deformation under a craniotomy. *Neurosurgery* **1998**, *43*, 514-526.
7. Hammoud, M.A.; Ligon, B.L.; Elsouki, R.; Shi, W.M.; Schomer, D.F.; Sawaya, R. Use of intraoperative ultrasound for localizing tumors and determining the extent of resection: a comparative study with magnetic resonance imaging. *Journal of neurosurgery* **1996**, *84*, 737-741.
8. Škrinjar, O.; Nabavi, A.; Duncan, J.J.M.i.a. Model-driven brain shift compensation. **2002**, *6*, 361-373.
9. Wittek, A.; Kikinis, R.; Warfield, S.K.; Miller, K. Brain shift computation using a fully nonlinear biomechanical model. In Proceedings of the International Conference on Medical Image Computing and Computer-Assisted Intervention, 2005; pp. 583-590.
10. Miga, M.I.; Sun, K.; Chen, I.; Clements, L.W.; Pheiffer, T.S.; Simpson, A.L.; Thompson, R.C.J.I.j.o.c.a.r.; surgery. Clinical evaluation of a model-updated image-guidance approach to brain shift compensation: experience in 16 cases. **2016**, *11*, 1467-1474.
11. Grunert, P.; Müller-Forell, W.; Darabi, K.; Reisch, R.; Busert, C.; Hopf, N.; Perneczky, A.J.C.A.S. Basic principles and clinical applications of neuronavigation and intraoperative computed tomography. **1998**, *3*, 166-173.
12. Nimsky, C.; Ganslandt, O.; Cerny, S.; Hastreiter, P.; Greiner, G.; Fahlbusch, R.J.N. Quantification of, visualization of, and compensation for brain shift using intraoperative magnetic resonance imaging. **2000**, *47*, 1070-1080.
13. Kuhnt, D.; Bauer, M.H.; Nimsky, C.J.C.R.i.B.E. Brain shift compensation and neurosurgical image fusion using intraoperative MRI: current status and future challenges. **2012**, *40*.
14. Clatz, O.; Delingette, H.; Talos, I.-F.; Golby, A.J.; Kikinis, R.; Jolesz, F.A.; Ayache, N.; Warfield, S.K. Robust nonrigid registration to capture brain shift from intraoperative MRI. *IEEE transactions on medical imaging* **2005**, *24*, 1417-1427.
15. Valdés, P.A.; Fan, X.; Ji, S.; Harris, B.T.; Paulsen, K.D.; Roberts, D.W.J.S.; neurosurgery, f. Estimation of brain deformation for volumetric image updating in protoporphyrin IX fluorescence-guided resection. **2010**, *88*, 1-10.
16. Trobaugh, J.W.; Richard, W.D.; Smith, K.R.; Bucholz, R.D. Frameless stereotactic ultrasonography: method and applications. *Computerized Medical Imaging and Graphics* **1994**, *18*, 235-246.
17. Roche, A.; Pennec, X.; Rudolph, M.; Auer, D.; Malandain, G.; Ourselin, S.; Auer, L.M.; Ayache, N. Generalized correlation ratio for rigid registration of 3D ultrasound with MR images. In Proceedings of the International Conference on Medical Image Computing and Computer-Assisted Intervention, 2000; pp. 567-577.
18. Koivukangas, J.; Ylitalo, J.; Alasaarela, E.; Tauriainen, A. Three-dimensional ultrasound imaging of brain for neurosurgery. *Annals of clinical research* **1986**, *18*, 65-72.
19. Farnia, P.; Ahmadian, A.; Shabanian, T.; Serej, N.D.; Alirezaie, J. Brain-shift compensation by non-rigid registration of intra-operative ultrasound images with preoperative MR images based on residual complexity. *International journal of computer assisted radiology and surgery* **2015**, *10*, 555-562.
20. Bayer, S.; Maier, A.; Ostermeier, M.; Fahrig, R.J.I.j.o.b.i. Intraoperative imaging modalities and compensation for brain shift in tumor resection surgery. **2017**, *2017*.
21. Farnia, P.; Mohammadi, M.; Najafzadeh, E.; Alimohamadi, M.; Makkiabadi, B.; Ahmadian, A. High-quality photoacoustic image reconstruction based on deep convolutional neural network: towards intra-operative photoacoustic imaging. *Biomedical Physics & Engineering Express* **2020**.
22. Pramanik, M.; Ku, G.; Li, C.; Wang, L.V. Design and evaluation of a novel breast cancer detection system combining both thermoacoustic (TA) and photoacoustic (PA) tomography. *Medical physics* **2008**, *35*, 2218-2223.
23. Mehrmohammadi, M.; Joon Yoon, S.; Yeager, D.; Y Emelianov, S.J.C.M.I. Photoacoustic imaging for cancer detection and staging. **2013**, *2*, 89-105.

24. Najafzadeh, E.; Ghadiri, H.; Alimohamadi, M.; Farnia, P.; Mehrmohammadi, M.; Ahmadian, A. Application of multi-wavelength technique for photoacoustic imaging to delineate tumor margins during maximum-safe resection of glioma: A preliminary simulation study. *Journal of Clinical Neuroscience* **2019**.
25. Arabpou, S.; Najafzadeh, E.; Farnia, P.; Ahmadian, A.; Ghadiri, H.; Akhoundi, M.S.A. Detection of Early Stages Dental Caries Using Photoacoustic Signals: The Simulation Study. *Frontiers in Biomedical Technologies* **2019**.
26. Moore, C.; Bai, Y.; Hariri, A.; Sanchez, J.B.; Lin, C.-Y.; Koka, S.; Sedghizadeh, P.; Chen, C.; Jokerst, J.V. Photoacoustic imaging for monitoring periodontal health: A first human study. *Photoacoustics* **2018**, *12*, 67-74.
27. Yan, Y.; John, S.; Ghalehnovi, M.; Kabbani, L.; Kennedy, N.A.; Mehrmohammadi, M.J.S.r. photoacoustic Imaging for Image-guided endovenous Laser Ablation procedures. **2019**, *9*, 1-10.
28. Petrova, E.; Brecht, H.; Motamedi, M.; Oraevsky, A.; Ermilov, S.J.P.i.M.; Biology. In vivo optoacoustic temperature imaging for image-guided cryotherapy of prostate cancer. **2018**, *63*, 064002.
29. Eddins, B.; Bell, M.A.L.J.J.o.b.o. Design of a multifiber light delivery system for photoacoustic-guided surgery. **2017**, *22*, 041011.
30. Wang, L.V.; Hu, S. Photoacoustic tomography: in vivo imaging from organelles to organs. *science* **2012**, *335*, 1458-1462.
31. Wang, L.V.; Yao, J. A practical guide to photoacoustic tomography in the life sciences. *Nature methods* **2016**, *13*, 627.
32. Attia, A.B.E.; Balasundaram, G.; Moothanchery, M.; Dinish, U.; Bi, R.; Ntziachristos, V.; Olivo, M. A review of clinical photoacoustic imaging: Current and future trends. *Photoacoustics* **2019**, 100144.
33. Beard, P. Biomedical photoacoustic imaging. *Interface focus* **2011**, *1*, 602-631.
34. Rosencwaig, A.; Gersho, A. Theory of the photoacoustic effect with solids. *Journal of Applied Physics* **1976**, *47*, 64-69.
35. Zackrisson, S.; Van De Ven, S.; Gambhir, S. Light in and sound out: emerging translational strategies for photoacoustic imaging. *Cancer research* **2014**, *74*, 979-1004.
36. Xu, M.; Wang, L.V. Photoacoustic imaging in biomedicine. *Review of scientific instruments* **2006**, *77*, 041101.
37. Farnia, P.; Najafzadeh, E.; Hariri, A.; Lavasani, S.N.; Makkiabadi, B.; Ahmadian, A.; Jokerst, J.V. Dictionary learning technique enhances signal in LED-based photoacoustic imaging. *Biomedical Optics Express* **2020**, *11*, 2533-2547.
38. Hoelen, C.; De Mul, F.; Pongers, R.; Dekker, A. Three-dimensional photoacoustic imaging of blood vessels in tissue. *Optics letters* **1998**, *23*, 648-650.
39. Raumonen, P.; Tarvainen, T. Segmentation of vessel structures from photoacoustic images with reliability assessment. *Biomedical optics express* **2018**, *9*, 2887-2904.
40. Najafzadeh, E.; Ghadiri, H.; Alimohamadi, M.; Farnia, P.; Mehrmohammadi, M.; Ahmadian, A. Evaluation of multi-wavelengths LED-based photoacoustic imaging for maximum safe resection of glioma: a proof of concept study. *International Journal of Computer Assisted Radiology and Surgery* **2020**.
41. Karthikesh, M.S.; Yang, X.J.E.B.; Medicine. Photoacoustic image-guided interventions. **2020**, *245*, 330-341.
42. Han, S.H.J.N. Review of photoacoustic imaging for imaging-guided spinal surgery. **2018**, *15*, 306.
43. Kubelick, K.P.; Emelianov, S.Y.J.U.i.M.; Biology. A Trimodal Ultrasound, Photoacoustic and Magnetic Resonance Imaging Approach for Longitudinal Post-operative Monitoring of Stem Cells in the Spinal Cord. **2020**, *46*, 3468-3474.
44. Iversen, D.H.; Wein, W.; Lindseth, F.; Unsgård, G.; Reinertsen, I. Automatic intraoperative correction of brain shift for accurate neuronavigation. *World neurosurgery* **2018**, *120*, e1071-e1078.
45. Reinertsen, I.; Descoteaux, M.; Siddiqi, K.; Collins, D.L. Validation of vessel-based registration for correction of brain shift. *Medical image analysis* **2007**, *11*, 374-388.
46. Chen, S.J.-S.; Reinertsen, I.; Coupé, P.; Yan, C.X.; Mercier, L.; Del Maestro, D.R.; Collins, D.L. Validation of a hybrid Doppler ultrasound vessel-based registration algorithm for neurosurgery. *International journal of computer assisted radiology and surgery* **2012**, *7*, 667-685.

47. Farnia, P.; Ahmadian, A.; Khoshnevisan, A.; Jaberzadeh, A.; Serej, N.D.; Kazerooni, A.F. An efficient point based registration of intra-operative ultrasound images with MR images for computation of brain shift; A phantom study. In Proceedings of the Engineering in Medicine and Biology Society, EMBC, 2011 Annual International Conference of the IEEE, 2011; pp. 8074-8077.
48. Arbel, T.; Morandi, X.; Comeau, R.M.; Collins, D.L. Automatic non-linear MRI-ultrasound registration for the correction of intra-operative brain deformations. In Proceedings of the International Conference on Medical Image Computing and Computer-Assisted Intervention, 2001; pp. 913-922.
49. Ji, S.; Hartov, A.; Roberts, D.; Paulsen, K. Mutual-information-corrected tumor displacement using intraoperative ultrasound for brain shift compensation in image-guided neurosurgery. In Proceedings of the Medical Imaging 2008: Visualization, Image-Guided Procedures, and Modeling, 2008; p. 69182H.
50. Wein, W.; Ladikos, A.; Fuerst, B.; Shah, A.; Sharma, K.; Navab, N. Global registration of ultrasound to MRI using the LC 2 metric for enabling neurosurgical guidance. In Proceedings of the International Conference on Medical Image Computing and Computer-Assisted Intervention, 2013; pp. 34-41.
51. Coupé, P.; Hellier, P.; Morandi, X.; Barillot, C. 3D rigid registration of intraoperative ultrasound and preoperative MR brain images based on hyperechogenic structures. *Journal of Biomedical Imaging* **2012**, *2012*, 1.
52. Rivaz, H.; Karimaghaloo, Z.; Collins, D.L. Self-similarity weighted mutual information: a new nonrigid image registration metric. *Medical image analysis* **2014**, *18*, 343-358.
53. Rivaz, H.; Chen, S.J.-S.; Collins, D.L. Automatic deformable MR-ultrasound registration for image-guided neurosurgery. *IEEE transactions on medical imaging* **2015**, *34*, 366-380.
54. Machado, I.; Toews, M.; George, E.; Unadkat, P.; Essayed, W.; Luo, J.; Teodoro, P.; Carvalho, H.; Martins, J.; Golland, P. Deformable MRI-ultrasound registration using correlation-based attribute matching for brain shift correction: Accuracy and generality in multi-site data. *NeuroImage* **2019**, *202*, 116094.
55. Zhang, Q.; Liu, Y.; Blum, R.S.; Han, J.; Tao, D. Sparse representation based multi-sensor image fusion for multi-focus and multi-modality images: A review. *Information Fusion* **2018**, *40*, 57-75.
56. Farnia, P.; Ahmadian, A.; Shabanian, T.; Serej, N.D.; Alirezaie, J. A hybrid method for non-rigid registration of intra-operative ultrasound images with pre-operative MR images. In Proceedings of the Engineering in Medicine and Biology Society (EMBC), 2014 36th Annual International Conference of the IEEE, 2014; pp. 5562-5565.
57. Farnia, P.; Makkiabadi, B.; Ahmadian, A.; Alirezaie, J. Curvelet based residual complexity objective function for non-rigid registration of pre-operative MRI with intra-operative ultrasound images. In Proceedings of the Engineering in Medicine and Biology Society (EMBC), 2016 IEEE 38th Annual International Conference of the, 2016; pp. 1167-1170.
58. Huang, K.; Aviyente, S. Sparse representation for signal classification. In Proceedings of the Advances in neural information processing systems, 2007; pp. 609-616.
59. Roozgard, A.; Barzigar, N.; Verma, P.; Cheng, S. 3D-SCoBeP: 3D medical image registration using sparse coding and belief propagation. *International Journal of Diagnostic Imaging* **2014**, *2*, 54.
60. Nam, S.; Davies, M.E.; Elad, M.; Gribonval, R. The cosparse analysis model and algorithms. *Applied and Computational Harmonic Analysis* **2013**, *34*, 30-56.
61. Zhou, N.; Jiang, H.; Gong, L.; Xie, X. Double-image compression and encryption algorithm based on co-sparse representation and random pixel exchanging. *Optics and Lasers in Engineering* **2018**, *110*, 72-79.
62. Kiechle, M.; Hawe, S.; Kleinsteuber, M. A joint intensity and depth co-sparse analysis model for depth map super-resolution. In Proceedings of the Proceedings of the IEEE international conference on computer vision, 2013; pp. 1545-1552.

63. Kiechle, M.; Habigt, T.; Hawe, S.; Kleinsteuber, M. A bimodal co-sparse analysis model for image processing. *International Journal of Computer Vision* **2015**, *114*, 233-247.
64. Han, C.; Zhang, H.; Gao, C.; Jiang, C.; Sang, N.; Zhang, L. A Remote Sensing Image Fusion Method Based on the Analysis Sparse Model. *IEEE Journal of Selected Topics in Applied Earth Observations and Remote Sensing* **2016**, *9*, 439-453.
65. Gao, R.; Vorobyov, S.A.; Zhao, H. Image fusion with cosparse analysis operator. *IEEE Signal Processing Letters* **2017**, *24*, 943-947.
66. Farnia, P.; Najafzadeh, E.; Ahmadian, A.; Makkiabadi, B.; Alimohamadi, M.; Alirezaie, J. Co-sparse analysis model based image registration to compensate brain shift by using intra-operative ultrasound imaging. In Proceedings of the 2018 40th Annual International Conference of the IEEE Engineering in Medicine and Biology Society (EMBC), 2018; pp. 1-4.
67. Ren, W.; Skulason, H.; Schlegel, F.; Rudin, M.; Klohs, J.; Ni, R. Automated registration of magnetic resonance imaging and optoacoustic tomography data for experimental studies. *Neurophotonics* **2019**, *6*, 025001.
68. Gehrung, M.; Tomaszewski, M.; McIntyre, D.; Disselhorst, J.; Bohndiek, S. Co-Registration of Optoacoustic Tomography and Magnetic Resonance Imaging Data from Murine Tumour Models. *Photoacoustics* **2020**, 100147.
69. Surry, K.; Austin, H.; Fenster, A.; Peters, T. Poly (vinyl alcohol) cryogel phantoms for use in ultrasound and MR imaging. *Physics in Medicine & Biology* **2004**, *49*, 5529.
70. Myronenko, A.; Song, X. Intensity-based image registration by minimizing residual complexity. *IEEE transactions on medical imaging* **2010**, *29*, 1882-1891.
71. Hawe, S.; Kleinsteuber, M.; Diepold, K. Analysis operator learning and its application to image reconstruction. *IEEE Transactions on Image Processing* **2013**, *22*, 2138-2150.
72. Cai, S.; Kang, Z.; Yang, M.; Xiong, X.; Peng, C.; Xiao, M.J.S. Image denoising via improved dictionary learning with global structure and local similarity preservations. **2018**, *10*, 167.
73. Zhang, Q.; Fu, Y.; Li, H.; Zou, J. Dictionary learning method for joint sparse representation-based image fusion. *Optical Engineering* **2013**, *52*, 057006.